Seismic tomography of the Excavation Damaged Zone of the Gallery 04 in the Mont Terri Rock Laboratory

Florence Nicollin, Dominique Gibert, Paul Bossart, Christophe Nussbaum, Céline Guervilly

Geophys. J. Int. (2008) **172,** 226–239 doi: 10.1111/j.1365-246X.2007.03615.x

Seismic tomography of the Excavation Damaged Zone of the Gallery 04 in the Mont Terri Rock Laboratory

F. Nicollin,[1] D. Gibert,[1] P. Bossart,[2] Ch. Nussbaum[3] and C. Guervilly[1,4]

[1]*Géosciences Rennes (CNRS/INSU UMR* 6118*) and GdR FORPRO (CNRS-ANDRA G*788*), Université Rennes* 1, *Bât.* 15, *campus de Beaulieu* 35042 *Rennes Cedex, France. E-mail: florence.nicollin@univ-rennes1.fr, gibert@univ-rennes 1.fr*

[2]*Federal Office for Topography, swisstopo, Seftigenstrasse* 264, 3084 *Wabern, Switzerland. E-mail: paul.bossart@swisstopo.ch*

[3]*Institut Géotechnique SA, route de la Gare* 65, 2882 *St-Ursanne, Switzerland. E-mail: christophe.nussbaum@geo-online.com*

[4]*Laboratoire de Géophysique Interne et Tectonophysique, Université Joseph Fourier,* BP 53, 38041 *Grenoble cedex* 9, *France. E-mail: celine.guervilly@obs.ujf-grenoble.fr*

Accepted 2007 September 11. Received 2007 September 11; in original form 2007 March 17

SUMMARY

An endoscopic antenna is used to perform a seismic cross-hole tomography in the Excavation Damaged Zone (EDZ) of the new G04 gallery of the Mont Terri Underground Rock Laboratory (Switzerland) excavated in Opalinus clay. More than 800 seismic traces were recorded between two vertical boreholes by combining 22 source and 48 receiver locations. A vertical area of 1.2×3.4 m under the floor of the gallery is investigated with a high-resolution tomography. Data with a very good quality allow to determine the traveltimes and the amplitudes of a 40 kHz source wavelet propagating between the two boreholes. The analysis of the traveltimes shows that the wave velocity is homogeneous but anisotropic with a minimum value of $2490 \pm 45\ \mathrm{m\,s^{-1}}$ in the direction normal to the bedding and a maximum of $3330 \pm 90\ \mathrm{m\,s^{-1}}$ parallel to the bedding. The amplitude of the first arrivals strongly varies depending on the source–receiver locations, and suggesting an heterogeneous distribution of the attenuation coefficient of the seismic waves. A Bayesian inversion provides likely models of attenuation that are compared with geological observations. The areas where fractures or cracks exist in the Opalinus clay appear as highly absorbing the seismic waves.

Key words: Inverse theory; Downhole methods; Tomography; Seismic anisotropy; Seismic attenuation; Acoustic properties.

1 INTRODUCTION

Argillaceous formations are aimed at being used for radioactive waste disposal because of their remarkable confinement and self-healing properties (e.g. Meier *et al.* 2000). To investigate the suitability of waste storage in these formations, the Mont Terri Underground Rock Laboratory (URL) was created in a Mesozoic shale formation constituted by the Opalinus clay (Fig. 1). Since 1995, the URL received numerous research programs (Thury & Bossart 1999; Bossart & Thury 2007) many of them devoted to the study of the Excavation Damaged Zone (EDZ) formed by a diffuse layer of fractured rock resulting from stress changes produced by the excavation of the galleries. The structure of the EDZ is controlled by the regional stress regime, the local tectonic, the stratigraphic conditions, the excavation technique, and the shape of the gallery (Bossart *et al.* 2002; Blümling *et al.* 2007). Several studies have been devoted to both the geomechanical and the transport properties of the EDZ in order to assess the safety of high-activity nuclear waste storage (Blümling *et al.* 2007; Bossart *et al.* 2002, 2004; Hunsche *et al.* 2004; Martin *et al.* 2004). In several studies, geophysical techniques have been successfully used to probe the EDZ, in particular electrical tomography provided images of the conductivity in large volumes of the EDZ (Kruschwitz & Yaramanci 2004; Gibert *et al.* 2006) and seismic methods provided both geometrical and geomechanical information in local areas (Schuster *et al.* 2001).

In the present study, we discuss a seismic cross-borehole tomography experiment performed with two vertical boreholes (BEZ-G1 and BEZ-G2) in the floor of the EZ-G04 area of new G04 gallery in the Mont Terri URL (Bossart & Thury 2007). The seismic endoscopy probe described by Nicollin *et al.* (2002) was used as the receiving antenna in the BEZ-G1 borehole to record the waves emitted by a source placed in the BEZ-G2 borehole. A total of 22 source depths and 48 receiver locations were used to obtain a set of 832 seismic traces whose ray paths sample a 2-D domain of 1.2 m in width and 3.4 m in height between the two boreholes (Fig. 2). Both the traveltime and the amplitude of the first arrivals were determined for all seismic traces.

The traveltimes do not show significant spatial variation of the *P*-wave velocity, but they indicate a clear anisotropy of velocity whose maximum value is parallel to the bedding. Using a ray tracing model, we verify that this anisotropy do not produce a significant curvature of the ray paths and that the straight-ray approximation remains valid. Strong variations of the amplitudes are observed depending on the considered ray path, and tomography models of the

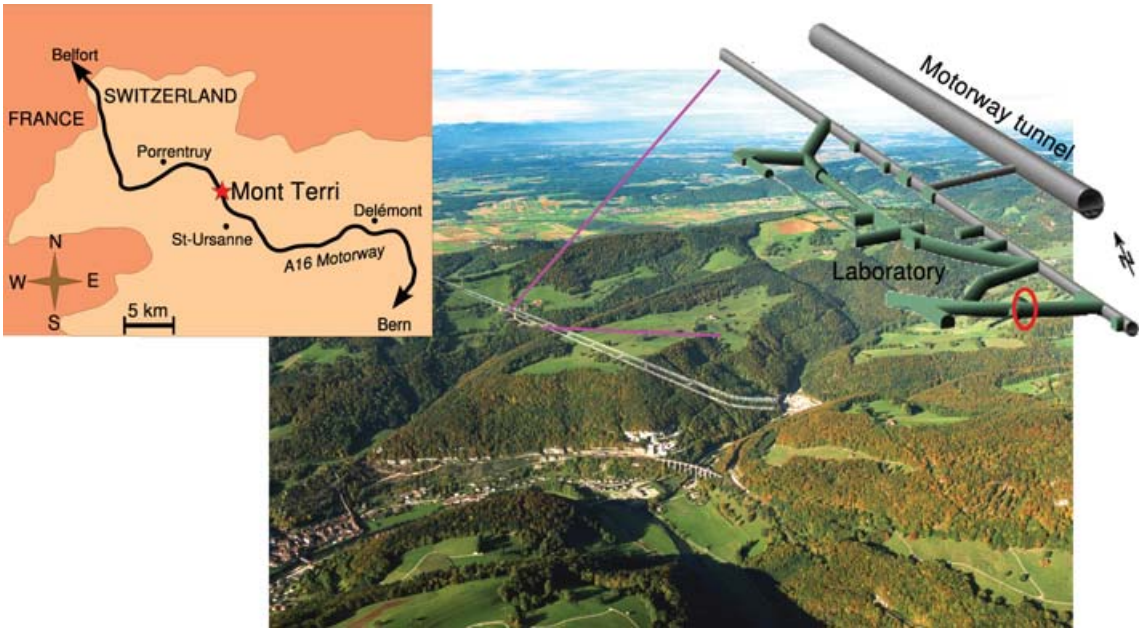

Figure 1. Geographical location of the Mont Terri Rock Laboratory, and detailed view of the galleries (the red circle shows the EZ-G04 experimental area).

attenuation coefficient are obtained by inverting the amplitude data and using straight rays. A non-linear Bayesian–Metropolis algorithm is used to obtain models whose posterior probability accounts for the variable quality of individual data. All models obtained show a pattern of alternatively absorbing and non-absorbing bands parallel to the direction of the bedding and with the highest value of the anisotropic attenuation close to the principal direction of the fractures.

2 FIELD EXPERIMENTS

2.1 Experimental setup

The seismic endoscope was designed and built at Géosciences Rennes (CNRS UMR 6118) to perform 3-D acoustic imaging at a metric scale around shallow-depth fluid-filled boreholes (Nicollin *et al.* 2002; Conil 2003). The body of the seismic endoscope is a cylinder of 10 cm in diameter and made with an acoustically absorbing foam. It is equipped with a piezo-electric isotropic source at its lower end and with 64 piezo-electric directional receivers placed every 7 cm along four generatrices located 90° apart along the cylindrical probe. The source–receiver distance varies from 0.5 to 1.55 m. The receivers have a receiving angle of about 30° and a bandwidth between 30 and 100 kHz which allows to record high-frequency seismic signals from a volume of a few meters in diameter around the borehole. The azimuthal sampling may be refined by rotating the probe by fractions of 90° with a stepping motor placed at the mouth of the borehole.

A controlled source signal is computed and transmitted to an arbitrary waveform generator to trigger the power amplifier connected to the piezo-electric source. The entire experimental setup is driven with a PXI® system using a computer code written with the LabView® language. The source signals were optimized during preliminary experiments done in our water tank and using the inversion technique of Conil *et al.* (2004) to account for the non-linear responses of the whole apparatus chain. This procedure ensures the constancy of both the shape and the amplitude, A_S, of the source signal. In the present study, this signal was a Ricker wavelet with a central frequency of 40 kHz, and the received seismic traces were sampled at 500 kHz during 2 ms from the shot time and digitized with a 12-bits A-D converter. To improve the signal-to-noise ratio, the traces shown in Fig. 3 were obtained by stacking one hundred individual traces recorded for a given source–receiver configuration.

The EZ-G04 experimental area is located in the start niche (i.e. the entrance) of the G04 gallery and is located at the southern end of the Mont Terri URL (Fig. 1). This start niche is oriented in a NW–SE direction and was excavated in the spring of 2004; the remaining part of the gallery was completed in autumn 2004. The two vertical boreholes (BEZ-G1 and BEZ-G2) were drilled in the floor of the gallery in March 2005 and they are located in the so-called EZ-G04 area beneath the electrode array used by Gibert *et al.* (2006), 50 cm to the SE from electrode ring *II*. The BEZ-G1 borehole is on the gallery axis and BEZ-G2 is 1.2 m apart to the NE. Both boreholes have a depth of 7 m and a diameter of 131 mm. A plastic tubing is placed at the mouth of the boreholes across the concrete invert (i.e. the first 50 cm). The boreholes were filled with a special synthetic oil (Radiagreen BDMF VLF) used in the Opalinus clay of Mont Terri to stabilize the walls. Periodic re-examinations of the state of the boreholes do not show any particular damage of the walls.

2.2 Measurement procedure

The tomography experiment was performed by placing the endoscope antenna in BEZ-G1 and the source in BEZ-G2 (Fig. 2). In the present experiment, a standard isotropic Bruël & Kjaer transducer with a 40 kHz nominal frequency was used for the source. A single line (i.e. the one turned towards BEZ-G2) of 16 receivers of the seismic endoscope is used to record the seismic traces, and the endoscope was successively placed at three depth locations to obtain 48 receiver positions $0.84 \leq z_R \leq 4.13$ m with a step of $\Delta z_R = 7$ cm. In BEZ-G2, the source was placed at 22 positions $0.81 \leq z_S \leq 4.17$ m with a step of $\Delta z_S = 16$ cm. The endoscope (i.e. the receivers) was positioned in the borehole with an accuracy of 1 mm, and the auxiliary source was positioned with an accuracy of a few

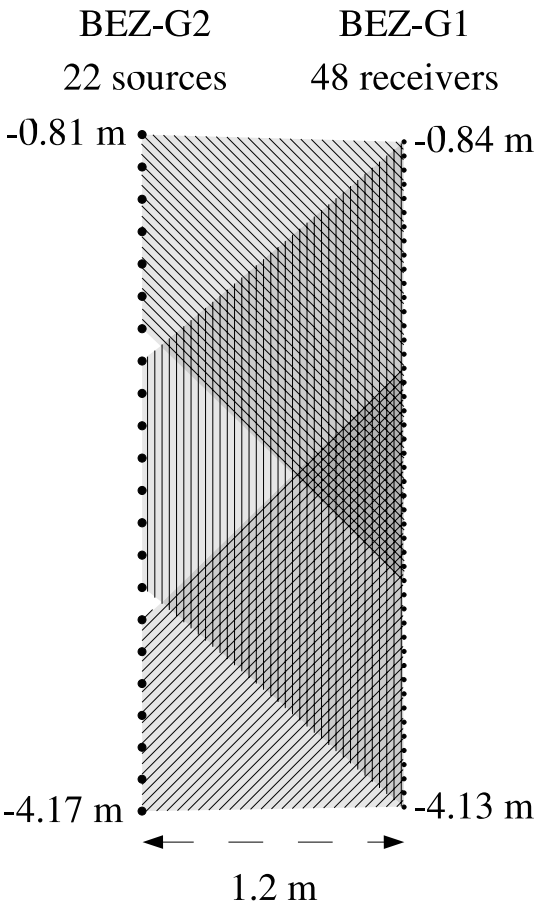

Figure 2. Experimental setup: 48 positions occupied by the receivers in the BEZ-G1 borehole every 7 cm, and 22 positions occupied by the source in the BEZ-G2 borehole every 16 cm. When the source is located at the 7 highest positions, the signal is recorded by the 32 highest receivers (oblique hatching's going down towards the right); when the source is located at the 8 intermediate positions, the signal is recorded by the 48 receivers (vertical hatching's); when the source is located at the 7 lowest positions, the signal is recorded by the 32 lowest receivers (oblique hatching's going up towards the right).

centimetres. Fig. 2 gives the details of the ray coverage corresponding to the tomographic arrangement of the present study: the seven uppermost/lowest source positions gave a detectable signal only at the 32 uppermost/lowest receivers. On the other hand, all the receivers were active when the signal was transmitted from the eight intermediate positions of the source. The whole experiment represents 832 source–receiver pairs which insonify the medium with paths of various length and various orientation.

3 DATA ANALYSIS

The data depend on the two spatial parameters (z_R, z_S) and on time t, and the representation of the 832 seismic traces on a single plot is not informative. Fig. 3 displays three common-shot gathers (z_R, t) for $z_S = 1.45$ m (a), $z_S = 3.37$ m (b) and $z_S = 2.73$ m (c). The only processing applied to the data shown in this figure is a zero-phase bandpass filter which rejects both the continuous component (low cut-off frequency at 5 kHz) and the high-frequency noise (high cut-off frequency at 65 kHz). Most traces have a good signal-to-noise ratio allowing an automatic picking of the first arrivals, and a manually guided picking was needed for several traces like those recorded at receiver depths $z_R \geq 1.54$ m when the source is located at $z_S = 2.73$ m (Fig. 3c). Both the arrival-time and the amplitude of the transmitted direct waves are thus measured for all 832 source–receiver pairs.

3.1 *P*-wave velocity anisotropy

Fig. 3 shows that the arrival-times are minimum at depths systematically larger than the source depth, suggesting a velocity anisotropy. This is confirmed in Fig. 4(a) where the velocity averaged along the ray paths is plotted versus the ray angle, θ_{ray}. All data fall within a narrow band and do not display any dispersion as a function of the source depth. The minimum velocity is 2490 ± 45 m s^{-1} normal to the bedding ($\theta_{\text{ray}} = -42^\circ$), and the maximum is 3330 ± 90 m s^{-1} parallel to the bedding ($\theta_{\text{ray}} = 45^\circ$). These values are in very good agreement with the data given by (Bock 2000) who reports 2620 ± 400 m s^{-1} normal to the bedding and 3410 ± 240 m s^{-1} parallel to the bedding.

A ray tracing modelling was done for anisotropic seismic velocity, and we observed that the ray paths obtained for the velocity values given above have no significant curvature. This test confirmed us that straight rays may safely be used in the tomography algorithm.

3.2 *P*-wave amplitude variations

The amplitudes corrected for geometrical spreading show a strong dispersion spanning three orders of magnitude (Fig. 4b). This dispersion suggests an important heterogeneity of the attenuation coefficients. It is much less important (i.e. less than one order of magnitude) for deep data [(z_R, z_S) ≥ 2 m, black dots], and is even more reduced for the negative ray angles (ray paths very oblique to the bedding).

Later in this paper, tomography models will be obtained by inverting the data amplitudes. This amplitude tomography implies that the data have been properly corrected for instrumental effects affecting the measured amplitudes. In the present experiment, the main effect to be accounted for is the antenna directivity of the endoscopic probe. Indeed, the open-space directivity measured in a large water tank (Conil 2003) shows that waves with an incidence larger than about 30° are strongly attenuated. However, further modellings performed by Conil (2003) revealed that the open-space directivity is strongly perturbed by the presence of the borehole and that the effective directivity of the endoscope antenna must consider the whole borehole-endoscope system. A realistic modelling of this complex system involves sophisticated 3-D numerical models and is beyond the scope of the present study. For this reason, we prefer to experimentally determine the directivity, f, of the borehole-endoscope system from the *in situ* tomography data.

3.3 Amplitude corrections

In an absorbing medium, the classical ray theory expresses the amplitude as,

$$A_k = \frac{A_S}{l(\theta_{\text{ray}})}\, f(\theta_{\text{ray}})\, \exp[-\overline{\alpha}_k\, l(\theta_{\text{ray}})], \tag{1}$$

where A_S is the unknown and constant amplitude at the source, l is the length of the k's ray path, f is the directivity coefficient whose value depends on the ray angle, θ_{ray}, and $\overline{\alpha}_k$ is the attenuation coefficient averaged along the ray path. In this experiment, the waves

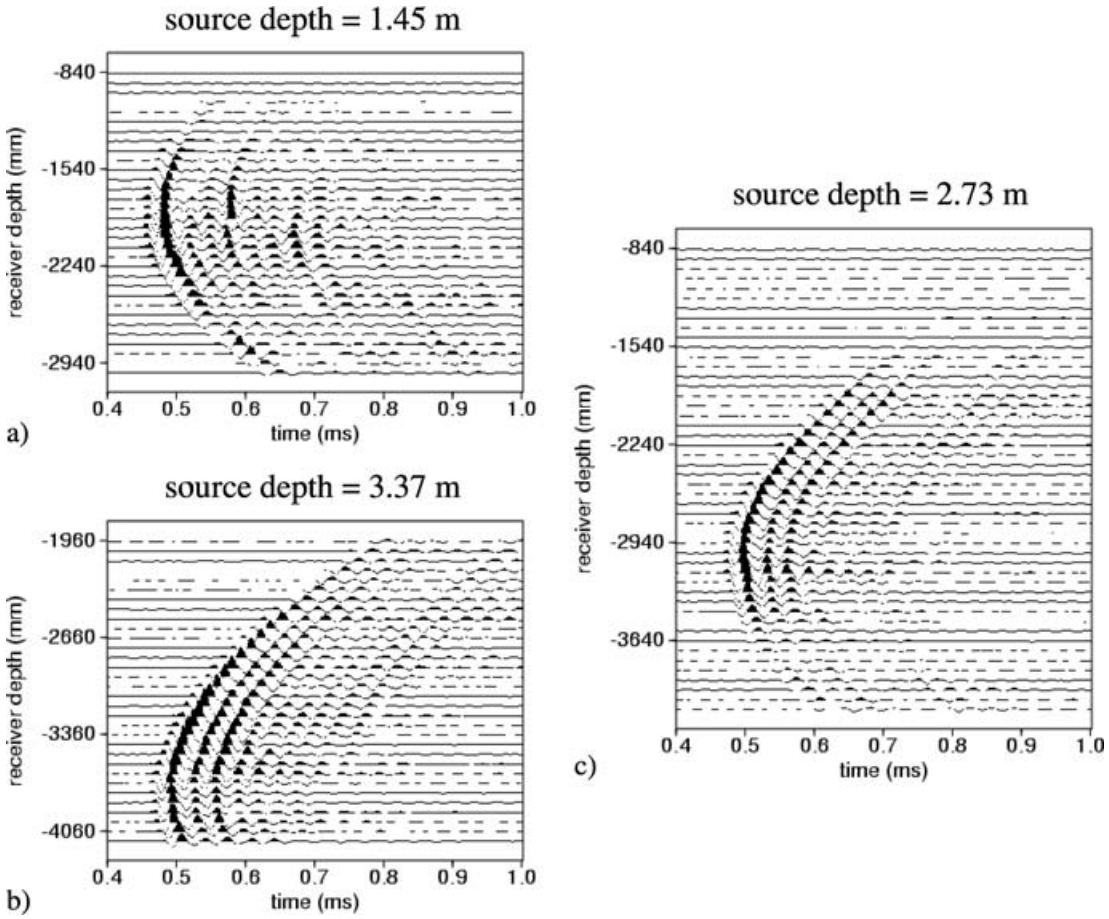

Figure 3. Raw data of the transmission tomography experiment gathered in common-shot for three source locations: (a) $z_S = 1.45$ m recorded by the 32 higher receivers; (b) $z_S = 3.37$ m recorded by the 32 lower receivers and (c) $z_S = 2.73$ m recorded by the 48 receivers.

propagating between the two parallel boreholes under same ray angle have same the ray path length. Then, the logarithm of the measured amplitudes corrected for geometrical spreading, may be written as,

$$\ln[A_k\, l(\theta_{\text{ray}})] = -\overline{\alpha}_k\, l(\theta_{\text{ray}}) + \ln f(\theta_{\text{ray}}) + \ln A_S. \tag{2}$$

In order to determine the directivity f from this equation, we use a data subset such that the average attenuation $\overline{\alpha}_k$ may be considered as a constant $\overline{\alpha}$. Relying on prior geological information and on Fig. 4(b), the retained data subset corresponds to the rays located in the deepest part of the boreholes, $(z_R, z_S) \geq 2$ m, and with a ray angle $\theta_{\text{ray}} \leq 0$. Indeed, as can be verified in the tomography images below, these rays are oblique enough to the structures to cross almost the same number of negative and positive absorbing regions (here we consider relative attenuation). For such rays, the constant-average $\overline{\alpha}$ hypothesis is expected to be acceptable.

To estimate $\overline{\alpha}$, we consider only the data for which $\theta_{\text{ray}} = -30^\circ \pm 8^\circ$, that is, such that both the ray paths are almost perpendicular to the structures and f may be considered constant within this narrow angular range. In this case, eq. (2) simplifies into,

$$\ln[A_k\, l(\theta_{\text{ray}})] = -\overline{\alpha}\, l(\theta_{\text{ray}}) + C \quad \text{for } \theta_{\text{ray}} = -30^\circ \pm 8^\circ, \tag{3}$$

where the constant $C = \ln f(-30^\circ) + \ln A_S$. Fig. 5(a) displays the corresponding data $\ln[A_k l(\theta_{\text{ray}})]$ versus the ray path length $l(\theta_{\text{ray}})$. The linear relation suggested by eq. (3) is actually observed in these data (black dots), and a linear fit gives $\overline{\alpha} = 1.77\ \text{m}^{-1}$. This value is used to correct all data for attenuation along the ray paths (Fig. 5b).

The median curve of the negative ray angles data (solid red line) is taken as the directivity curve $f(\theta_{\text{ray}} \leq 0)$ shifted by the $\ln A_S$ term. Assuming an even directivity, the full curve is obtained by letting $f(\theta_{\text{ray}} \geq 0) = f(-\theta_{\text{ray}})$ (dashed red line).

A final correction applied to the data concerns the suppression of the unknown but constant source amplitude, A_S (see eq. 2). In practice, this is done by dividing the measured amplitudes by $\overline{A}_0 = A_S {l_0}^{-1} f_0 \exp[-\overline{\alpha} l_0]$, the median value of the data for which $(z_R, z_S) \geq 2$ m and $\theta_{\text{ray}} = 0$. Fig. 4(c) shows the amplitudes corrected for all effects, namely geometrical spreading, directivity of the endoscope-borehole system, and source amplitude. With these corrections applied, the reduced amplitudes are modelled as,

$$\widetilde{A}_k = \frac{A_k\, l_k\, {f_k}^{-1}}{\overline{A}_0\, l_0\, {f_0}^{-1}} = \exp[\overline{\alpha}\, l_0 - \overline{\alpha}_k\, l_k], \tag{4}$$

where l_0 is the ray path length and f_0 the experimental directivity for $\theta_{\text{ray}} = 0$.

4 MODELS OF ATTENUATION COEFFICIENTS

According to the definition of the reduced amplitudes, and if the attenuation coefficient is spatially varying eq. (4) becomes,

$$\widetilde{A}_k = \exp\left[\overline{\alpha}\, l_0 - \int_{\mathcal{L}_k} \alpha(l)\, \mathrm{d}l\right], \tag{5}$$

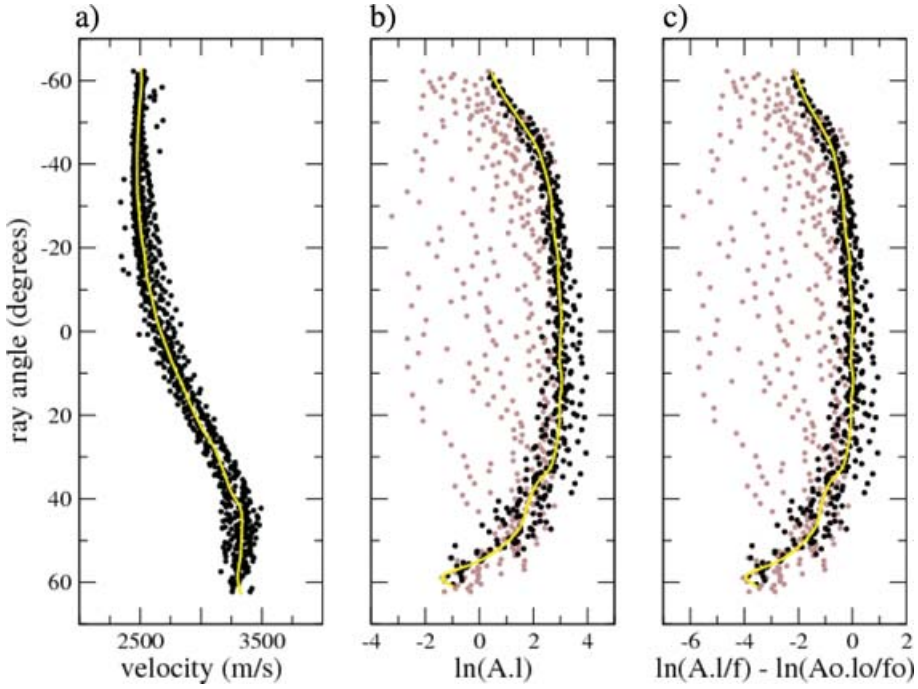

Figure 4. *P*-wave velocity and amplitude versus ray angle; negative ray angles correspond to upgoing waves from the BEZ-G2 source-borehole to the BEZ-G1 receivers-borehole, that is, following directions very oblique to the bedding. (a) Velocity computed from the arrival-times picked on the whole data and considering straight ray paths (black dots); median curve computed on θ_{ray} classes of 5° width (solid yellow line). (b) Logarithm of the amplitude corrected for geometrical spreading, measured at the first peak picked on the whole data (grey dots) and on selected data such that $(z_R, z_S) \geq 2$ m (black dots and solid yellow line for their median curve). (c) Same as (b) after directivity correction and normalization by the amplitude at $\theta_{\text{ray}} = 0$.

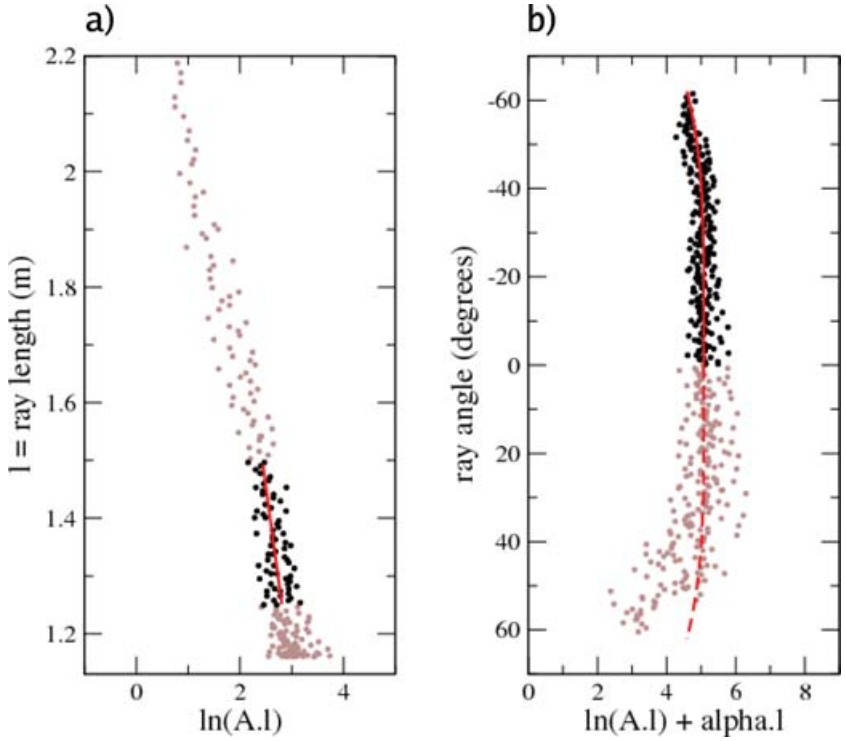

Figure 5. (a) Logarithm of the amplitude corrected for geometrical spreading versus ray paths length l, for data such that $(z_R, z_S) \geq 2$ m and $\theta_{\text{ray}} \leq 0$ (grey dots). The data such that $\theta_{\text{ray}} = -30° \pm 8°$, that is, 1.25 m $\leq l \leq$ 1.5 m, used to determine $\overline{\alpha}$ according to eq. (3), are shown as black dots. A linear fit on this data subset (solid red line) gives $\overline{\alpha} = 1.77\,\text{m}^{-1}$. (b) Logarithm of the amplitude corrected for both geometrical spreading and constant attenuation, $\overline{\alpha} = 1.77\,\text{m}^{-1}$, versus ray angles. The median curve of the subset such that $(z_R, z_S) \geq 2$ m and $\theta_{\text{ray}} \leq 0$ (black dots) gives the directivity function $f(\theta_{\text{ray}})$ (solid red line), which is assumed to be even (dashed red line for $\theta_{\text{ray}} \geq 0$).

where $\mathcal{L}_k$ represents the ray path corresponding to the k's amplitude of the data set. As stated above, the traveltimes analysis demonstrates that the straight ray paths may be safely used. In the following section, this model is used to determine 2-D distribution of the attenuation coefficient by inverting the reduced amplitude $\widetilde{A}_k$.

4.1 Discretization of the medium

Both the z_S and the z_R define the domain where the tomographic reconstruction of the attenuation coefficient may be done. This domain is a rectangular area of size $\Delta x = 1.2$ m by $\Delta z = 3.4$ m. Since the sources and the receivers were placed in the BEZ-G2 and BEZ-G1 boreholes, respectively, the geometry of the tomographic disposal is non-symmetrical and the medium is not uniformly sampled by the seismic rays. This can be observed in Fig. 6(a) which displays the density of the rays in square cells of about 13 cm. Strong differences exist inside the domain, especially between the intermediate depths where numerous rays cross each cell and the top and bottom parts where the cells count much less rays.

The inhomogeneities observed in the ray-coverage density (Fig. 6a) imply that the resolution varies from place to place in the tomographic domain. In order to account for this inhomogeneous resolution we discretize the attenuation model according to the ray sampling. The size of the cells used to represent the spatial distribution of the attenuation coefficient can be determined from the resolving kernels associated with the actual ray distribution. Let us recall that a resolving kernel, $K(x, z|x_a, z_a)$, is the reconstructed tomographic image of a point anomaly $\delta(x - x_a, z - z_a)$ located at (x_a, z_a) in the reference model taken here as homogeneous. The resolving kernels were computed according to the method proposed by Menke (1984) and the rays were given the width of the first Fresnel zone computed for a wavelength $\lambda = 7$ cm. In the present study, the resolving kernels are used to provide a rough estimate of the resolution, and we do not consider the fine sensitivity variations inside the Fresnel zone as recently evidenced by (Marquering *et al.* 1999; Dahlen *et al.* 2000; Hung *et al.* 2000; Dahlen and Baig 2002). Two examples of resolving kernels are shown in Figs 6(b) and (c). The kernel shown in Fig. 6(b) is located in an area of the tomographic domain where the ray coverage is both poor and anisotropic. As expected, the resulting resolving kernel has a wide extent indicating that the resolution in this part of the model will be coarse. The kernel shown in Fig. 6(c) corresponds to a domain where the ray density is high with a wide angular coverage. Here, the kernel has a point-like appearance indicating that the resolution in this part of the tomographic domain is excellent.

The resolving kernels were used to derive the size of the cells representing the distribution of the attenuation coefficient. In practice, we computed the inertial tensor of the kernels to obtain their equivalent elliptical sizes (Bracewell 1978). These elliptical sizes give an indication of the minimum spatial scale resolved in each part of the tomographic domain. In the present study, we represent the attenuation model by a set, $\mathcal{P}$, of discrete points, $P_i = (x_i, z_i)$, with attenuation α_i and distributed according to the resolution given by the resolving kernels. A total of 74 points has been defined at the centres of the cells of the irregular grid shown in Fig. 7. In Fig. 6(d), both the density and the orientation of the straight rays are displayed in this chosen grid, showing that all the cells contain an equivalent quantity of information. The parameters of the attenuation model to be determined take place at the centre of the cells thus defined.

The points P_i are used to interpolate the attenuation coefficient everywhere in the tomographic domain in order to solve the forward problem which gives the synthetic amplitudes to be compared with the data. In the present study, the interpolation is done on a fine grid of 23 per 67 meshes, that is, square meshes of about 5 cm side (see Fig. 10 where three models with the 74 parameters placed on the irregular broad grid are presented in top, and the associated interpolated models are displayed in bottom). The interpolation of the parameters is realized using the Akima method which performs bivariate interpolation from points irregularly distributed in the plane (Akima 1974).

4.2 Bayesian inversion of the amplitudes

Although eq. (5) shows that the inversion of the amplitudes to determine the attenuation coefficients is a linear problem when written in terms of the logarithm of the amplitude, we chose a Monte Carlo Bayesian formulation of the inverse problem in order to both estimate the degree of reliability of likely models and take into account the quality of each data, that is, its signal-to-noise ratio.

Two kind of models are used below, one with an isotropic attenuation coefficient and the other with an anisotropic attenuation tensor. The isotropic model vector is formed with the scalar attenuation values at the $N = 74$ points P_i and is defined as,

$$\mathbf{m} = \{\alpha_1, \alpha_2, \ldots, \alpha_N\}. \tag{6}$$

As explained above, these points are used to obtain an interpolated distribution of the attenuation coefficient necessary for the forward problem. The anisotropic model is defined on the same point set $\mathcal{P}$ and reads,

$$\mathbf{m} = \left\{ \alpha_{a_1}, \alpha_{a_2}, \ldots, \alpha_{a_N}, \left[\frac{\alpha_a - \alpha_b}{\alpha_a}\right]_1, \left[\frac{\alpha_a - \alpha_b}{\alpha_a}\right]_2, \ldots, \left[\frac{\alpha_a - \alpha_b}{\alpha_a}\right]_N, \theta_{\alpha_1}, \theta_{\alpha_2}, \ldots, \theta_{\alpha_N} \right\}, \tag{7}$$

where α_a indicates the maximum value of attenuation, α_b the minimum value, and θ_α the angle between the direction of maximum attenuation and the x axis.

The data vector, **d**, is made of the logarithm of the reduced amplitude of the first arrivals picked on the 832 experimental seismic traces. As noted in Section 3, the detection of the first arrival is sometimes difficult for signals with a low signal-to-noise ratio. The data errors are estimated from the variability of the reduced amplitude, measured on seismic traces recorded at nearby receivers and by assuming that one trace and its two neighbours (same source and two adjacent receivers) correspond to an identical attenuation-path and should have the same amplitude. The reduced amplitudes are divided into four classes, each counting nearly the same number of elements: the lowest amplitudes $[\ln(\widetilde{A}) < -1.96]$, the low amplitudes $[-1.96 \leq \ln(\widetilde{A}) < -0.92]$, the high amplitudes $[-0.92 \leq \ln(\widetilde{A}) < -0.24]$ and the highest amplitudes $[\ln(\widetilde{A}) \geq -0.24]$. Then, we compute the distribution of the distances $\{\ln(\widetilde{A}) - \overline{\ln(\widetilde{A})}\}$, where $\overline{\ln(\widetilde{A})}$ is the average value of three adjacent traces. The usage of the logarithm implies that twice the amplitude and half the amplitude give the same distance. Fig. 8 presents the distribution obtained for the four classes: thanks to the logarithm, the curves have symmetrical shape, and as expected, the higher the amplitude the narrower the statistical distribution. In the remaining, these experimentally determined distributions are interpreted as probability density functions, and they are used in the

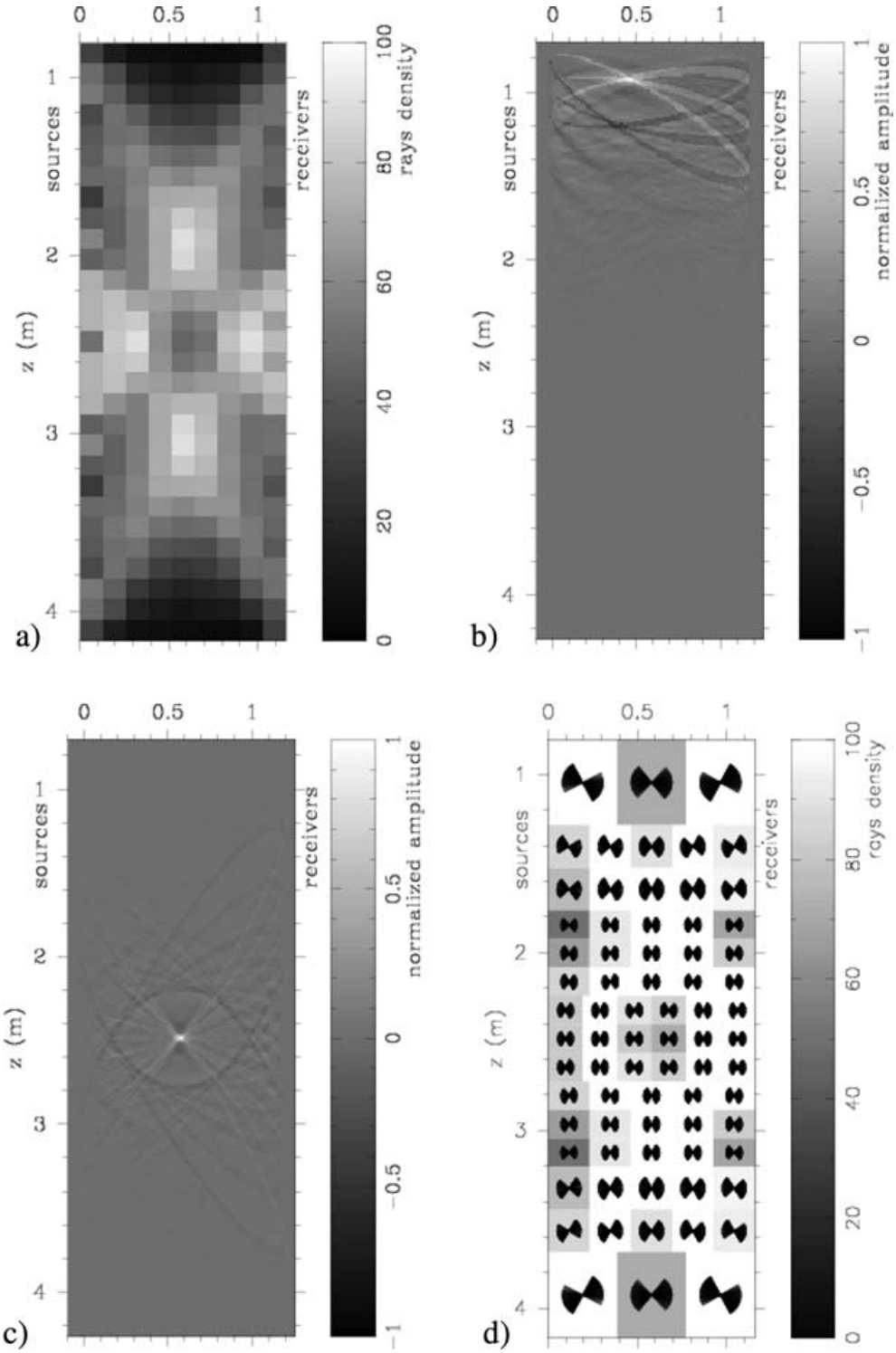

Figure 6. Lighting of the medium assuming straight ray paths: (a) ray-coverage density calculated on a regular grid of 9 per 29 rectangular cells; (b) and (c) two of the 261 (9 × 29) resolving kernels computed taking into account the Fresnel zone and (d) density and orientation of the rays in varying meshes whose size is optimized.

Bayesian selection of the models during the iterations of the Monte Carlo inversion.

In practice, the model selection relies on the following likelihood function,

$$L(\mathbf{m}) \propto P(\mathbf{d} - \mathbf{d}_\mathbf{m}), \tag{8}$$

where $\mathbf{d}_\mathbf{m}$ is the synthetic data vector produced by the interpolated version of the model $\mathbf{m}$, and P symbolically represents the probability densities experimentally determined from the data and shown in Fig. 8. As discussed above, a particular probability density curve is selected as a function of the log-amplitude. The search for the acceptable models is performed with the Metropolis algorithm which

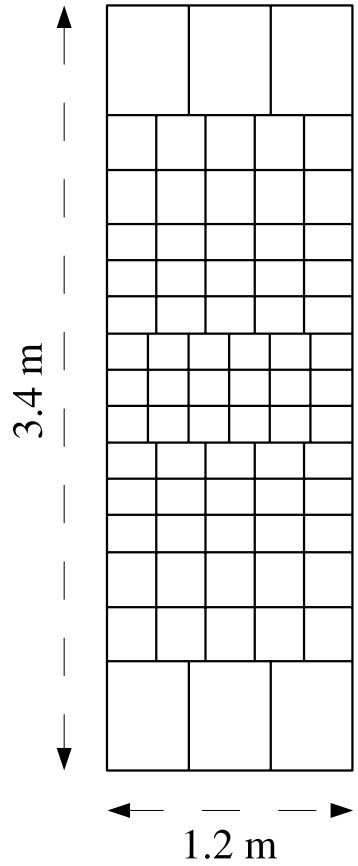

Figure 7. Discretization of the 2-D medium between the two boreholes: the size of the cells is set in order to homogenize the resolution, based on the density and orientation of the rays and on the resolving kernels shown in Fig. 6.

generates a sequence of models distributed according to eq. (8) (Metropolis *et al.* 1953; Bhanot 1988; Sambridge & Mosegaard 2002). The sequence of models is incrementally constructed, and the next model, $\mathbf{m}_{j+1}$, to be added in the sequence is chosen according to the random choice,

$$\text{prob}\left[\mathbf{m}_{j+1} = \mathbf{m}_{\text{try}}\right] = \min\left[1, \frac{L(\mathbf{m}_{\text{try}})}{L(\mathbf{m}_j)}\right], \tag{9}$$

where $\mathbf{m}_j$ is the last model incorporated in the sequence and $\mathbf{m}_{\text{try}}$ is a candidate model which may eventually be included in the sequence. Eq. (9) indicates that a more-likely model is always accepted and that a less-likely model is sometimes accepted. When the random assignment given by Eq. (9) fails, that is, when the less-likely candidate model is rejected, the replication formula $\mathbf{m}_{j+1} = \mathbf{m}_j$ is used instead. By this way, the sequence of models is guided towards the regions of the models space where the likelihood is maximum (see Fig. 9). The candidate model, $\mathbf{m}_{\text{try}}$, is obtained by perturbing the current model $\mathbf{m}_j$, in order to give some memory to the Metropolis chain and to make the algorithm not a simple Monte Carlo search. One of the parameter is randomly selected among all the elements of the current model, and it is randomly perturbed in a limited range. This range of perturbation is chosen so that 50 per cent of the candidate models are accepted according to eq. (9).

4.3 Practical issues

The inversion of isotropic models defined by eq. (6) involves the determination of the $N_I = 74$ parameters α_j from the 832 reduced amplitudes, $\widetilde{A}_k$, and using the forward problem given by eq. (5) with $\overline{\alpha} = 1.77\,\text{m}^{-1}$. The inversion process starts with a uniform model whose attenuation value is set to $\alpha = 1.77\,\text{m}^{-1}$. Fig. 9 shows the evolution of the likelihood of the models accepted in the sequence during the model selection performed by the Metropolis algorithm. An important increase of the likelihood is observed during the first

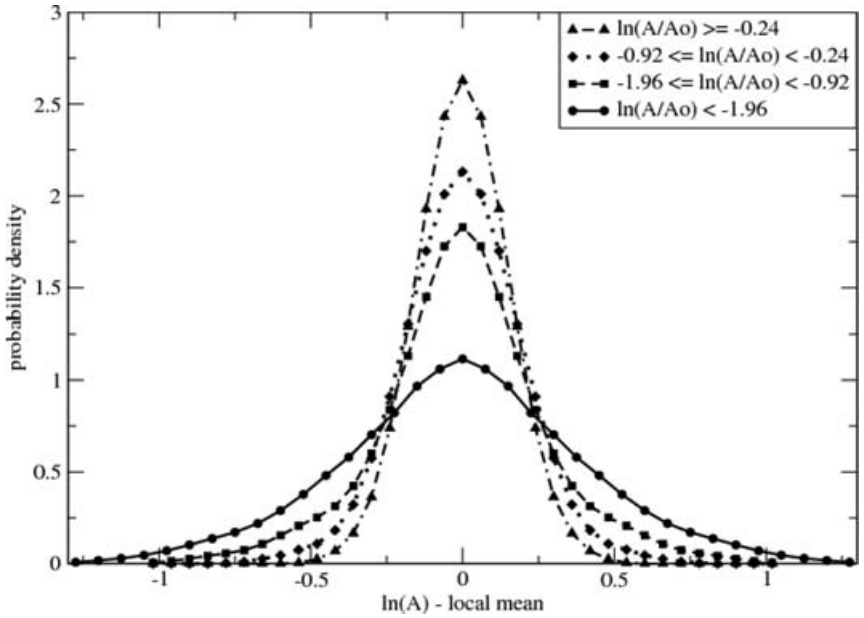

Figure 8. Estimation of the variability of the data: distribution of the distance between the reduced amplitude and the average value obtained on three adjacent traces. We assume that one trace and its two neighbours correspond to a same attenuation-path. The distances are computed using the logarithm of the amplitude so that double and half give the same absolute difference. The highest amplitudes [$\ln(\widetilde{A}) \geq -0.24$] create the sharpest peak (i.e. the best signal-to-noise ratio) while the lowest amplitudes [$\ln(\widetilde{A}) < -1.96$] create the widest peak (i.e. the worst signal-to-noise ratio).

5000 iterations until a plateau is reached where that the likelihood fluctuates around an average value. The sequence produced during this later stage corresponds to a stochastic equilibrium where the Metropolis chain performs an importance sampling of the models according to their posterior probability. The inversion process is stopped after 50 000 iterations.

The inversion of anisotropic attenuation models involves the search for the maximum value of attenuation, α_a, the minimum value of attenuation, α_b, and the direction θ_α of maximum attenuation (eq. 7). The inverse problem then consists in determining $N_A = 222$ parameters from the 832 amplitude data. A modified anisotropic version of eq. (5) is used to calculate the synthetic data vector $\mathbf{d}_\mathrm{m}$ by taking into account the orientation of the straight rays respect to the ellipse of anisotropy in each mesh of the fine grid. As for the isotropic inversion, $\overline{\alpha} = 1.77\,\mathrm{m}^{-1}$ in eq. (5), and the initial model is a uniform isotropic one with $\alpha_a = \alpha_b = 1.77\,\mathrm{m}^{-1}$. The likelihood of the models obtained for the anisotropic inversion increases less quickly than the likelihood of isotropic models (plateau reached after about 40 000 iterations, see Fig. 9), but it reaches higher values after the first 20 000 iterations. This better fit may be explained by the fact that the number of parameters is three times greater for the anisotropic models than for the isotropic ones. The results of both the isotropic and anisotropic inversions are presented in the next section.

5 RESULTS AND DISCUSSION

5.1 Isotropic inversion

A series of 50 inversions has been performed according to the protocol explained above. Each inversion was done with a different seed number of the random generator used to perturb the models of the Metropolis chain, and all likelihood curves look very similar to the average curve displayed in grey in Fig. 9. The likelihood of the final model of each sequence varies by about 0.3 per cent from one run to another. This means that the 50 final models, despite their differences, have the same degree of reliability with respect to the data.

Fig. 10 presents three of these 50 final models, chosen to show the strongest variations observed between models. The top part of the figure represents the final 74 α_i's placed at their corresponding P_i's, and the interpolated attenuation distributions are presented at the bottom of the figure. These interpolated distributions correspond to the models actually used to calculate the synthetic data. The differences between the 50 models are very small, the greatest ones being observed in the top and in the bottom of the tomographic domain where the resolution is the worst (see Fig. 6).

The average and standard deviation of the 50 interpolated models are computed and shown in Fig. 11. In the average model, the attenuation coefficient α varies between $0.3\,\mathrm{m}^{-1}$ and $6.9\,\mathrm{m}^{-1}$, with a global mean value equal to $2.1\,\mathrm{m}^{-1}$. The standard deviation varies between 8 and 44 per cent of the mean average attenuation, with a global mean value of about 20 per cent. The main features visible in the average model consist in strong attenuation areas located in the top of the domain, on the BEZ-G2 source-borehole side (left-hand side in Fig. 11), and along two oblique and narrow bands that extent from the top of the BEZ-G2 source-borehole (left-hand side) to the bottom of the BEZ-G1 receivers-borehole (right-hand side).

5.2 Anisotropic inversion

Following the same procedure as for the isotropic inversions, a series of 50 anisotropic inversions was performed with a different grain of the random generator for each run. The likelihood of the final model of each Metropolis sequence varies by about 0.7 per cent and it is significantly larger than the likelihood of the final isotropic models (see Fig. 9). Fig. 12 shows the average (top) and the standard deviation (bottom) of the 50 interpolated models.

The distribution of maximum attenuation, α_a, appears very similar to the one of the isotropic attenuation coefficient, varying between 0.5 and $6.8\,\mathrm{m}^{-1}$, with a global mean value $\overline{\alpha_a}$ equal to $2.3\,\mathrm{m}^{-1}$ (Fig. 12a). Especially the areas of high attenuation are recovered: top of the domain, BEZ-G2 side, and oblique bands dipping towards BEZ-G1. The standard deviation of α_a, shown in Fig. 12(d), is slightly larger than the one of the isotropic attenuation since it varies between 14 and 48 per cent of $\overline{\alpha_a}$) with most values around 25 per cent.

The degree of anisotropy is given by the flatness $(\alpha_a - \alpha_b)/\alpha_a$ which varies between 0 and 0.5 with a global mean value, $\overline{(\alpha_a - \alpha_b)/\alpha_a}$, equal to 0.25 (Fig. 12b). The image of anisotropy appears rather homogeneous in most of the domain, except for the top and bottom part where the more restricted range of the ray angle may introduce a bias in the anisotropy (see Fig. 6). The standard deviation of anisotropy (Fig. 12e) appears homogeneous with values ranging from 31 to 70 per cent of $\overline{(\alpha_a - \alpha_b)/\alpha_a}$.

Fig. 12(c) shows the distribution of the third model parameter, θ_α, the direction of maximum attenuation projected in the tomographic plane. It exhibits an oblique band of positive angles, that is, dipping towards the SSE (right-hand side of the image), in coincidence with the narrow bands of high attenuation observed in Fig. 12(a). In that area, θ_α is around 20°. As observed for the degree of anisotropy, the standard deviation of θ_α is rather homogeneous in the whole tomographic domain and varies between 14° and 45° (Fig. 12f).

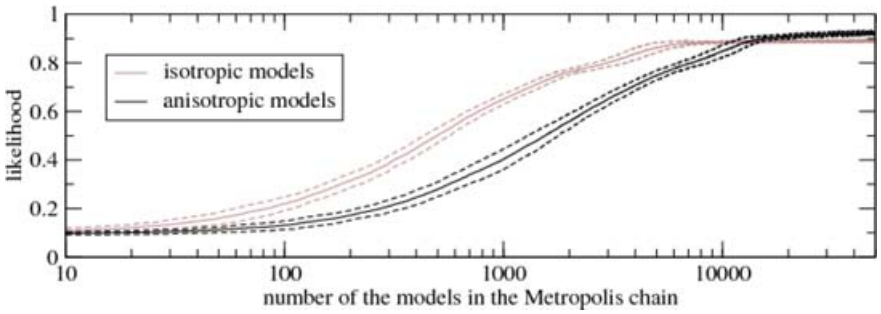

Figure 9. Likelihood curves of the models forming the Metropolis chain. The average curve of 50 isotropic inversions is plotted in grey solid line with its variability $\pm\,\sigma$ (the standard deviation) plotted in grey dashed lines, the average curve of 50 anisotropic inversions and its variability are plotted in black solid and dashed lines.

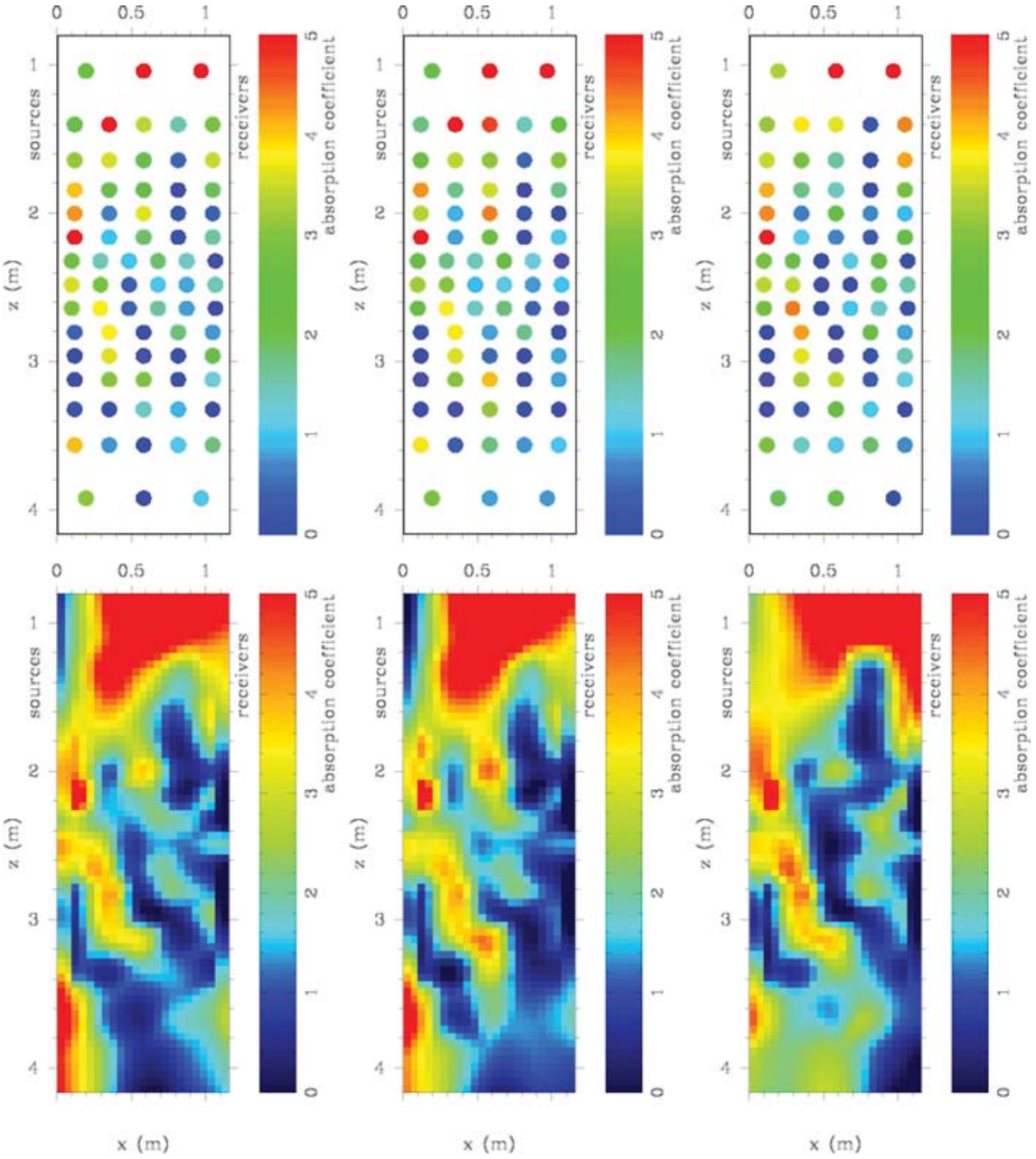

Figure 10. Three likely models of attenuation coefficient between the two boreholes. High attenuation values are displayed in red while low attenuation values are displayed in blue. Top: models of the 74 parameters retained by the inversion; bottom: interpolated models used to calculate the synthetic data.

During the anisotropic inversion, we observed that the three types of parameters (maximum attenuation, anisotropy and direction of maximum attenuation) are not equally resolved. The best resolved parameter is the maximum attenuation as confirmed by its low variability shown in Fig. 12(d) (average uncertainty of about 25 per cent). The anisotropy coefficient is less well resolved with an average uncertainty of about 50 per cent (Fig. 12e). The direction of maximum attenuation is the most fluctuating parameter during the Metropolis iterations, (see Fig. 12f).

5.3 Comparison with geological data

A detailed small-scale structural survey has been carried out during the excavation of the G04 gallery and later on the cores extracted from the BEZ-G boreholes. All structural data indicate that two families of tectonic fractures are visible. The first family of fractures is shown in blue in Fig. 13 and is characterized by steep (dip of 48°) and extended (> 5 m) fractures parallel to the bedding. The second family of fractures is shown in red in Fig. 13 and is formed by short (about 1 m) splay fractures with a moderate dip of about 15°. The fracture frequency in the BEZ-G1 borehole is higher than in BEZ-G2, and the correlation of fractures from one borehole to the other is not possible excepted for the fractures marked (d) in Fig. 13.

The most conspicuous feature visible in both the isotropic (Fig. 11) and anisotropic (Fig. 13) models of attenuation is a strong attenuation area located in the top of the domain where an EDZ produced by the excavation of the gallery may be expected and where

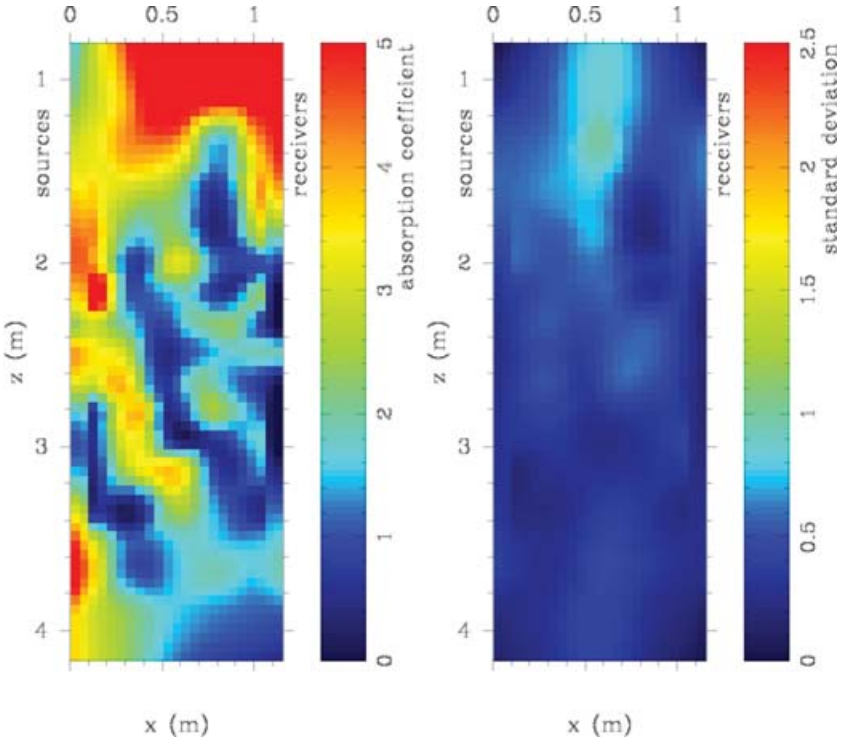

Figure 11. Interpolated model of attenuation coefficient between the two boreholes. Left-hand side: average values obtained from 50 likely models (high attenuation values are displayed in red while low attenuation values are displayed in blue). Right-hand side: standard deviation to the mean values. Note that the range of the colour scale used to represent the average model is twice larger than the one used to represent the standard deviation.

many fractures were observed in the extracted cores. The side of the tomographic domain located near the BEZ-G2 borehole also appears as a high attenuating zone, despite a lower number of fractures observed in the cores extracted from this borehole. However, this feature may be correlated with the results of electrical tomography that showed the presence of higher resistivity in the northern side of the floor of the gallery, revealing there a more damaged zone (Gibert *et al.* 2006). Also clearly visible in the models of attenuation is an oblique structure consisting of two highly attenuating bands [marked (a) and (b) in Fig. 13] separated by a band with a low attenuation. These bands have a global inclination identical to the one of the bedding planes and the first family of fractures in blue, as depicted on Fig. 13. However, some kicks are observed along these bands with a less-inclined direction more similar to the one of the second family of fractures. A third less continuous band marked (c) in Fig. 13 might also correspond to a well-developed bedding plane as no fracture was observed in either borehole. In the whole oblique structure, the direction of maximum attenuation, third parameter of the anisotropic inversion, is also close to the structural directions (see Fig. 12c).

Although the structural data are not sufficient to enable a strong correlation with the features visible in the tomographic reconstructions of the attenuation distribution, there is a good agreement between the inclinations of both the fractures and the attenuating bands. We may then safely consider that the zones of the tomographic domain where the attenuation is high are areas of tectonic discontinuities or well-developed bedding planes. The high resolution achieved in the central part of the tomographic domain allows to reveal small-scale patterns in the attenuation distribution. The patches with high attenuation, as those marked (a), (b) and (c) in Fig. 13, may correspond to tectonic fault planes and well-developed bedding planes where the attenuation is probably due to wave scattering.

6 CONCLUSIONS

The seismic tomography experiments discussed in the present study were performed at high frequency (40 kHz) and at metric spatial scales. The use of the seismic endoscope as an antenna and of a controlled source signal allows to obtain high-quality data from which traveltime and relative attenuation were determined. The main results obtained in the present paper are as follows.

(i) The experimental traveltimes do not indicate any significant variation of the wave velocity in the domain, but they reveal an anisotropy with a minimum velocity, $2490 \pm 45\,\mathrm{m\,s^{-1}}$, normal to the bedding, and a maximum velocity, $3330 \pm 90\,\mathrm{m\,s^{-1}}$, parallel to the bedding. These *P*-wave velocities fall within the velocity interval found in the Mont Terri Laboratory (Thury 2002), are coherent with the values (2700–$2800\,\mathrm{m\,s^{-1}}$) found by Schuster *et al.* (2001) for undisturbed clay, and are in very good agreement with the values ($2620 \pm 400\,\mathrm{m\,s^{-1}}$ normal to the bedding and $3410 \pm 240\,\mathrm{m\,s^{-1}}$ parallel to the bedding) reported by Bock (2000).

(ii) The amplitude of the first arrivals strongly varies and may have abrupt variations between nearby seismic traces. The amplitudes of the first arrivals may vary by more than two orders of magnitude depending on the region considered in the tomographic domain. Such variations of amplitudes were also observed by Schuster *et al.* (2001).

(iii) The discretization of the attenuation models is constrained by the characteristic size of the resolving kernels in order to account for the inhomogeneous ray coverage of the tomographic domain.

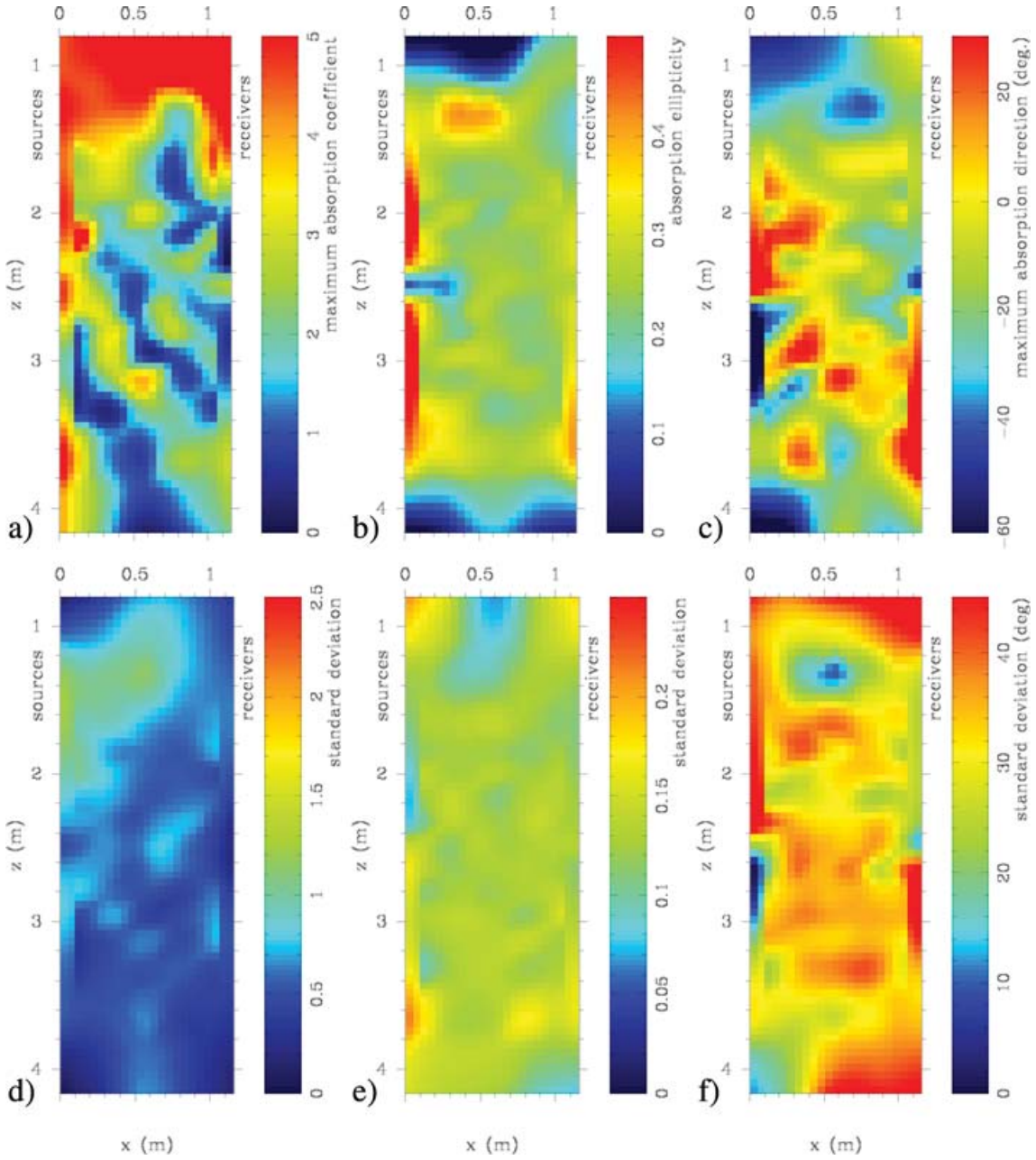

Figure 12. Interpolated model of anisotropic attenuation coefficient between the two boreholes. Top: average values obtained from 50 likely models of the three parameters: (a) coefficient of maximum attenuation (high values in red, low values in blue), (b) anisotropy of attenuation (isotropic attenuation in blue, anisotropic attenuation with a flatness of 0.5 in red) and (c) direction of the maximum attenuation from the *x*-axis [positive angles correspond to directions towards the bottom from BEZ-G2 (left-hand side) to BEZ-G1 (right-hand side)]. Bottom: standard deviation to the mean values for the three parameters: (d) maximum attenuation, (e) anisotropy flatness and (f) anisotropy direction. Note that the ranges of the colour scale used to represent the average values are twice larger than the ones used to represent the related standard deviation.

(iv) Both an isotropic and an anisotropic model of attenuation have been used to recover the attenuation distribution. The results obtained for both models are similar and coherent.

(v) The use of a Bayesian Monte Carlo method (i.e. the Metropolis algorithm) allows to assess the non-uniqueness of the inverted models.

(vi) A comparison between the inverted attenuation distributions and the geological observations indicates that the attenuating band-like features observed in the tomographic images coincide with a higher fracture frequency.

ACKNOWLEDGMENTS

This work benefited from invaluable help from the whole staff of the FORPRO GdR: *Joël Lancelot, Annie Le Bauzec, Patrick Pinettes* and *Patrick Verdoux* and from colleagues from ANDRA: *Patrick Lebon and Jacques Delay*. The seismic endoscope was built at Géosciences Rennes by *Frédéric Conil*, with the financial support of the Fonds National pour la Science, and the maintenance of the experimental device is now ensured by *Bruno Kergosien* from Géosciences Rennes. This work is financially supported by the CNRS and ANDRA through the GdR FORPRO and corresponds to the

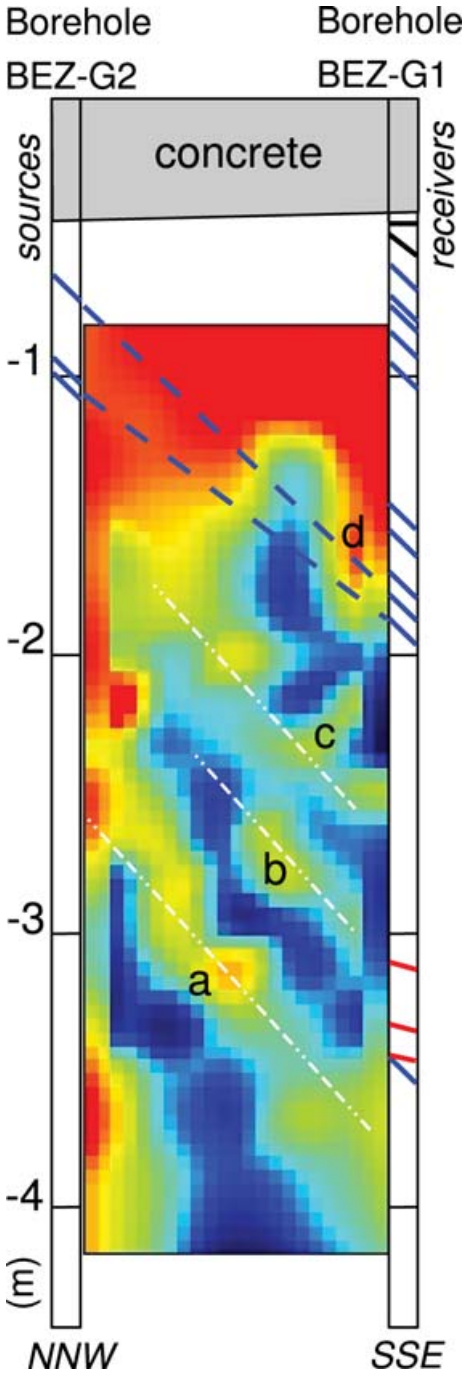

Figure 13. Sketch of the different structural features observed and expected in the tomographic domain. The oblique lines drawn in the two boreholes correspond to fractures observed in the extracted cores. The dashed lines drawn between the boreholes are hypothetical tectonic fractures. The tomographic image of the maximum attenuation of the anisotropic model is shown for comparison (same colour scale as in Fig. 12a).

GdR FORPRO contribution number 2007/03 A. This iPGP contribution 2286. Financial support of the experimental work at Mont Terri was provided by the NF-PRO European program. Detailed information concerning the Mont Terri Rock Laboratory may be found at http://www.mont-terri.ch. Great thanks to Associate Editor *Jean Virieux*, and to three anonymous reviewers for their constructive remarks that allowed us to improve our manuscript.

REFERENCES

Akima, H., 1974. Bivariate interpolation and smooth surface fitting based on local procedures, *Commun. ACM*, **17,** 26–31.

Bhanot, G., 1988. The metropolis algorithm, *Rep. Prog. Phys.*, **51,** 429–457.

Blümling, P., Bernier, F., Lebon, P. & Martin, C.D., 2007. The excavation damaged zone in clay formations time-dependent behaviour and influence on performance assessment, *J. Phys. Chem. Earth*, **33,** 588–599.

Bock, H., 2000. *RA-Experiment Rock Mechanics Analysis and Synthesis: Conceptual Model of Opalinus Clay*, Mont Terri Report, TR 2000-02s.

Bossart, P. & Thury, M., 2007. Research in the Mont Terri Rock laboratory: quo vadis? *J. Phys. Chem. Earth*, **32,** 19–31.

Bossart, P., Meier, P., Moeri, A., Trick, T. & Mayor, J.-C., 2002. Geological and hydraulic characterisation of the excavation disturbed zone in the Opalinus clay of the Mont Terri Rock Laboratory, *Eng. Geol.*, **66,** 19–38.

Bossart, P., Trick, T., Meier, P. & Mayor, J.-C., 2004. Structural and hydrogeological characterisation of the excavation-disturbed zone in the Opalinus clay (Mont Terri Project, Switzerland), *Appl. Clay Sci.*, **26,** 429–448.

Bracewell, R.N., 1978. *The Fourier Transform and it's Applications*, McGraw-Hill, New York.

Conil, F., 2003. Développements instrumentaux et expérimentation en endoscopie sismique, *Thèse de doctorat*, Université de Rennes 1, 249 pp.

Conil, F., Gibert, D. & Nicollin, F., 2004. Non-linear synthesis of input signals in ultrasonic experimental setups, *J. Acous. Soc. Am.*, **115**(1), 246–252.

Dahlen, F.A. & Baig, A.M., 2002. Fréchet kernels for body-wave amplitudes, *Geophys. J. Int.*, **150,** 440–466.

Dahlen, F.A., Hung, S.-H. & Nolet, G., 2000. Fréchet kernels for finite-frequency traveltimes—I. Theory, *Geophys. J. Int.*, **141,** 157–174.

Gibert, D., Nicollin, F., Kergosien, B., Bossart, P., Nussbaum, C., Grislin-Mouëzy, A., Conil, F. & Hoteit, N., 2006. Electrical tomography monitoring of the excavation damaged zone of the gallery 04 in the Mont Terri Rock Laboratory: field experiments and preliminary results, *Appl. Clay Sci.*, **33,** 21–34.

Hung, S.-H., Dahlen, F.A. & Nolet, G., 2000. Fréchet kernels for finite-frequency traveltimes—II. Examples, *Geophys. J. Int.*, **141,** 175–203.

Hunsche, U., Walter, F. & Schnier, H., 2004. Evolution and failure of the Opalinus clay: relationship between deformation and damage, experimental results and constitutive equation, *Appl. Clay Sci.*, **26,** 403–411.

Kruschwitz, S. & Yaramanci, U., 2004. Detection and characterization of the disturbed rock zone in claystone with the complex resistivity method, *J. appl. Geophys.*, **57,** 63–79.

Marquering, H., Dahlen, F.A. & Nolet, G., 1999. Three-dimensional sensitivity kernels for finite-frequency traveltimes: the banana–doughnut paradox, *Geophys. J. Int.,* **137,** 805–815.

Martin, D., Lanyon, G.W., Bossart, P. & Blümling, P., 2004. *Excavation Disturbed Zone (EDZ) in Clay Shale: Mont Terri*, Mont Terri Report, TN 2001-01.

Meier, P., Trick, Th., Blümling, P. & Volckaert, G., 2000. Self-healing of fractures within the EDZ at the Mont Terri Rock Laboratory: results after one year of experimental work, in *Proceedings of International Workshop on Geomechanics, Hydromechanical and Thermohydro-mechanical Behaviour of Deep Argillaceous Rocks: Theory and Experiment*, October 11–12th, 2000, Paris.

Menke, W., 1984. The resolving power of cross-borehole tomography, *Geophys. Res. Lett.*, **11,** 105–108.

Metropolis, N., Rosenbluth, A., Rosenbluth, N., Teller, A. & Teller, E., 1953. Equation of the state calculations by fast computing machines, *J. Chem. Phys.,* **21,** 1087–1092.

Nicollin, F., Conil, F. & Gibert, D., 2002. Seismic endoscopy: multi-offset multi-azimuth imaging around boreholes, data processing and experimental results, *Geophys. Prospect.*, **50,** 475–485.

Sambridge, M. & Mosegaard, K., 2002. Monte Carlo methods in geophysical inverse problems, *Rev. Geophys.*, **40**(3) 1009, doi:10.1029/2000RG00089.

Schuster, K., Alheid, H.-J. & Böddener, D., 2001. Seismic investigation of the excavation damaged zone in Opalinus clay, *Eng. Geol.*, **61,** 189–197.

Thury, M., 2002. The characteristics of the Opalinus clay investigated in the Mont Terri underground rock laboratory in Switzerland, *C. R. Physique*, **3,** 923–933.

Thury, M. & Bossart, P., 1999. The Mont Terri rock laboratory, a new international research project in a Mesozoic shale formation, in Switzerland, *Eng. Geol.*, **52,** 347–359.